Journal of Biomedical Optics

BiomedicalOptics.SPIEDigitalLibrary.org

Phase and amplitude correction in polygon tunable laser-based optical coherence tomography

Jinyu Fan
Pinghe Wang
Feng Gao
Zhehao Hu
Wen Kong
Haiwen Li
Guohua Shi

SPIE.

Jinyu Fan, Pinghe Wang, Feng Gao, Zhehao Hu, Wen Kong, Haiwen Li, Guohua Shi, "Phase and amplitude correction in polygon tunable laser-based optical coherence tomography," *J. Biomed. Opt.* **22**(9), 096013 (2017), doi: 10.1117/1.JBO.22.9.096013.

Phase and amplitude correction in polygon tunable laser-based optical coherence tomography

Jinyu Fan,[a] Pinghe Wang,[b] Feng Gao,[a] Zhehao Hu,[c] Wen Kong,[d] Haiwen Li,[a] and Guohua Shi[a,b,*]
[a]Chinese Academy of Sciences, Suzhou Institute of Biomedical Engineering and Technology, Jiangsu Key Laboratory of Medical Optics, Suzhou, China
[b]University of Electronic Science and Technology of China, School of Optoelectronic Information, Chengdu, China
[c]Zhejiang University, College of Optical Science and Engineering, Hangzhou, China
[d]China Jiliang University, College of Optical and Electronic Technology, Hangzhou, China

Abstract. Phase instability is a serious problem in swept-source optical coherence tomography (OCT) with polygon tunable lasers; however, these devices have additional issues. We found that polygon tunable lasers also have fluctuations in output power and sweep range: the former creates artifacts that may impair the recognition of sample information, and the latter reduces the interference signal utilization during phase correction. We demonstrate a method that uses the calibration signal to quantify these problems and improve system stability and image quality. The proposed amplitude correction and phase correction methods are used to eliminate vertical artifacts and improve the resolution of OCT flow and intensity images while reducing the phase error. [DOI: 10.1117/1.JBO.22.9.096013]

Keywords: optical coherence tomography; tunable laser; phase stability; biomedical imaging.

Paper 160861RRR received Dec. 21, 2016; accepted for publication Aug. 23, 2017; published online Sep. 23, 2017.

1 Introduction

Swept-source optical coherence tomography (SS-OCT) has higher sensitivity and scan speeds and is less prone to fringe washout[1,2] compared to spectral domain OCT. Therefore, SS-OCT is predominantly used in experimental research and biomedical imaging.

The core device of an SS-OCT system is a swept light source. High-speed swept light sources are primarily based on tunable filters, which are subdivided into polygon-scanner-based filters, microelectromechanical system-based filters, and fiber Fabry–Perot tunable filters. A polygon-scanner-based tunable filter splits the light via a grating and selects a frequency using the angle between the mirror and the incident light.[3] Polygon tunable lasers have been widely used for many years, and they exhibit good wavelength linearity over time.[4]

Nevertheless, the mechanical scan in a swept light source may cause differences among each period and degrade the image quality. Phase instability is one of the primary problems that affect functional OCT methods that depend on phase information, such as phase-resolved Doppler OCT[5] and optical microangiography (OMAG).[6] Hence, phase instability has been a research focus, and some researchers have proposed reducing this impact by adding a stationary mirror or glass plate to the sample arm,[7–9] whereas others suggest aligning interference signals.[10–12]

However, we determined that the difference in polygon mirrors causes phase instability and also output power and sweep range fluctuation in a polygon tunable laser. This creates vertical artifacts that can impair the recognition of samples and reduce interference signal utilization during phase correction, which will reduce the image axial resolution. Here, we use Mach–Zehnder interferometer (MZI) signals and Hilbert transforms to address these problems and demonstrate a phase correction method to apply to polygon tunable lasers-based OCT. We also normalized the amplitude of the interference signals and improved the contrast of tissue images. The theoretical analysis indicates that the phase information of the MZI signal and interference signals can be fully utilized in the proposed method, and the axial resolution of the flow and intensity images is improved while the phase-resolved Doppler image and OMAG also show good phase stability.

2 Measurement and Analysis of Laser Instability

We used a typical polygon tunable laser (HSL-2000, Santec Inc., Japan; center wavelength $\lambda_0 = 1315$ nm, scan range $\Delta\lambda = 110$ nm, measured peak output power from 10.36 to 13.19 mW, measured coherence length = 3.47 mm, measured duty rate from 72% to 79%, and measured scan rate 20 kHz) as our measured swept light source. The system included an integrated Michelson interferometer (MSI) (INT-MSI-1300, Thorlabs, Newton, New Jersey) and an integrated MZI (INT-MZI-1300, Thorlabs, Newton, New Jersey). The light from the source was split into the MSI and MZI at the ratio 95:5. After detection, the signals from MZI and MSI were recorded using a 14-bit resolution dual-channel data acquisition (DAQ) board (PCI5122, 100 MHz, National Instruments, Austin Texas) at a 50-MHz sampling rate. Each wavelength sweep consisted of 2048 samples. The DAQ was synchronized with the analog signal generation board (NI PCI6221, National Instruments, Austin Texas), which also generated the voltage waves that controlled the XY scanner. These devices were controlled using software written in C++. The schematic of our OCT system is shown in Fig. 1.

2.1 *Instability of Sweep Range and Output Power*

The relative sweep range and output power were measured using the MZI signals. The light at each end of the signal disappears.

*Address all correspondence to: Guohua Shi, E-mail: ioe_eye@126.com

1083-3668/2017/$25.00 © 2017 SPIE

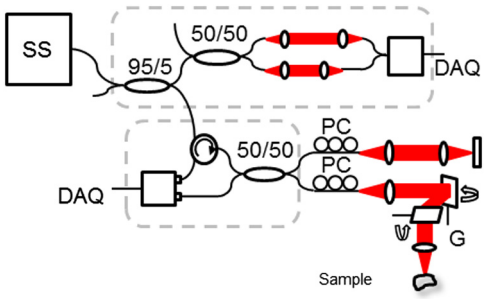

Fig. 1 Schematic of SS-OCT system. SS, swept source; G, galvanometric scanner; and PC, polarization controller

The output power also varied (see Fig. 2, where two MZI signals are aligned using the offsets calculated by cross correlation).

The signals we acquired were not linear in k-space, and their relationship is presented by the unwrapped phase curves of their Hilbert transforms, which are frequently used to resample the interference signal.[11,13,14] The beginning and ending phases of the curve determined the sweep range in k-space, and their positions determined the sweep range in the time domain (see unwrapped phase curve in Fig. 2). The average optical power in one sweep cycle determines the amplitude of the A-line; therefore, amplitude fluctuation can be described by relative output power, which can be obtained from the mean value of the envelope curve—amplitude of the Hilbert transform of the MZI signal.

We acquired three sets of MZI signals from each polygon tunable laser, and each set contained 1000 A-lines. The relative change ratios of sweep range for the wavenumber and time domain points were 7.16% and 7.76%, respectively, and the amplitude change ratio was 28.68%, as shown in Fig. 3.

To calculate the relative offset values in the time domain, we also implemented cross correlation between the reference MZI signal and other MZI signals. Figure 3(b) indicated that both had a fluctuation frequency of 660 Hz for the output power and sweep range, and each fluctuation cycle contained 30 sweep cycles (A-lines), which took 1.5 ms. Therefore, it was evident that fluctuation in output power, sweep range, and spectral misaligned (phase instability) was derived from periodic scans of the polygon mirror in the laser.

2.2 *Impacts on Image Quality*

To show the impact of output power fluctuation and phase instability, the fixed-pattern noise and a paperboard were included in our sample. Fixed-pattern noise is a type of coherence noise derived from the optical components of the device; it always appears as horizontal lines across the image.[15] However, these horizontal lines seemed truncated in our intensity image [Fig. 4(a)]. The paperboard had a simple structure, but the cross section of the image also displayed vertical artifacts [Fig. 4(b)]. This phenomenon causes problems in the recognition of sample information.

We found that the indices of peak amplitude of MZI signals corresponded to the fringe positions in the image. Therefore, vertical noise occurs due to output power fluctuation.

A larger shift in the spectra also causes phase instability and affects the phase-resolved Doppler image as shown in Fig. 4(c).

3 Digital Signal Processing and Imaging

To obtain the offset values between the A-lines in the time domain, cross correlations between the reference MZI signal and other MZI signals were implemented, and the A-lines were subsequently aligned by shifting these values. The phase error caused by misplacement can be represented by $\Delta\varphi_{m_s} = -\frac{2\pi z m_s}{N}$, where m_s is the misplaced point in k-space, z is the depth of sample, and N is the total number of wavenumber samples.[12] The delays among different MZI signals were not integer multiples of the sampling interval; thus, after integer pixels shift, some misplacement may still remain in the time domain, $m_t = 1/2$. To simply demonstrate the relationship between m_s and m_t, we assumed wavelength distribution in wavenumber domain was approximately linear with that in time domain, and thus, there was $m_s \approx cm_t$, in which $c = N/N_t$ and N_t was the effective signal point number in time domain. Then, the residual phase error range can be described as $\Delta\varphi_{rms} \in (-\frac{\pi cz}{N}, \frac{\pi cz}{N})$. In this research, the value of constant c was 1.059.

To improve the precision of the alignment, we interpolated and extended the MZI signals and A-lines by zero-padding in the frequency domain before performing the cross correlation and shift, and then aligned A-lines were obtained by downsampling the aligned extended A-lines. Finally, the residual phase error range could be described as $\Delta\varphi_{rms} \in (-\frac{\pi cz}{NM}, \frac{\pi cz}{NM})$, where

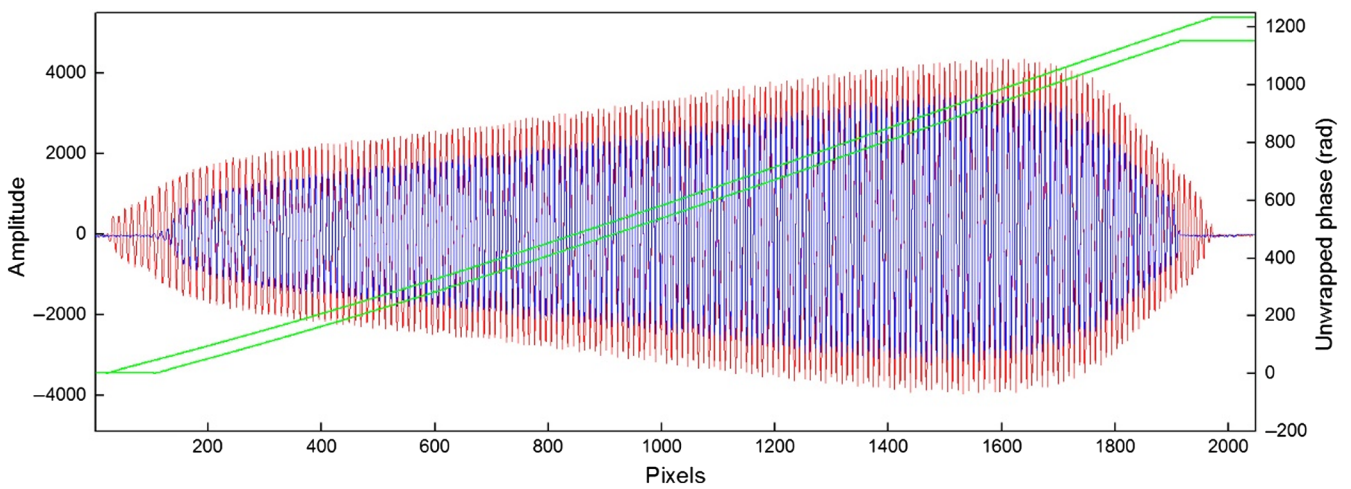

Fig. 2 Two aligned MZI signals and corresponding unwrapped phase curves (green curves).

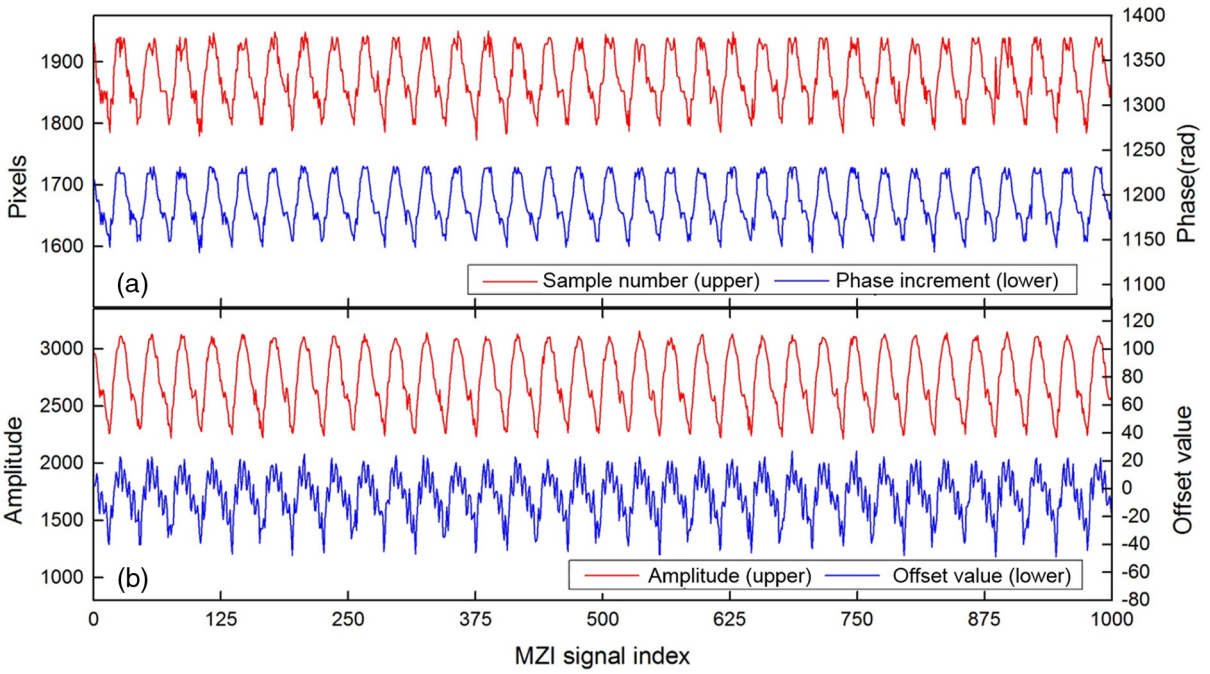

Fig. 3 Analysis of the MZI signals: (a) differences between the beginning and ending position in time domain and wavenumber (unwrapped phase) domain and (b) mean amplitude of the envelope and relative offset values of reference MZI signal and other MZI signals.

M is an extension multiple, and the possible phase error value was reduced.

The alignment accuracy can be described by the standard deviation of the phase differences (phase noise) between the reference MZI signal and other MZI signals that were aligned. Figure 5(a) demonstrates the relationship between the extension multiple and phase noises obtained from 6000 MZI signals, which indicates that the noise quickly decreased with increasing extension multiples when the extension multiple was <16. However, the noise reached a lower limit when the multiple was larger than 40.

The aligned unwrapped phase curves of the MZI signal obtained by performing Hilbert transforms are plotted in Fig. 5(b), in which they were distributed in eight curves with different initial wavelengths and indicated that the sweep range changed at specific values rather than at random values. The polygon tunable laser had a consistent wavelength distribution at different sweep cycles because all phase curves were parallel to each other. Hence, all aligned MZI signals had the same unwrapped phase distribution, and all aligned A-lines can be resampled to a linear k-space utilizing only the reference MZI signal. In this process, the reference MZI signal was that with a maximum sweep range, so A-lines with a larger sweep range do not require truncation and the full length can be fully used.

This method is shown schematically in Fig. 6. The remaining steps included fixed-pattern noise subtraction, fast Fourier transformation (FFT), and image mapping.

The relative amplitudes obtained from the measurement method described in Sec. 2.1 were used to scale the sample signals and correct the amplitude of intensity images. Normalization could be implemented before or after the FFT.

3.1 *Amplitude Correction in Intensity Image*

We normalized the fixed-pattern noise and paperboard image mentioned above, and these vertical artifacts were completely eliminated, as shown in Figs. 7(b) and 7(e).

Although intensity images were normalized, phase-resolved Doppler images were still completely wrong [Figs. 7(c) and 7(f)].

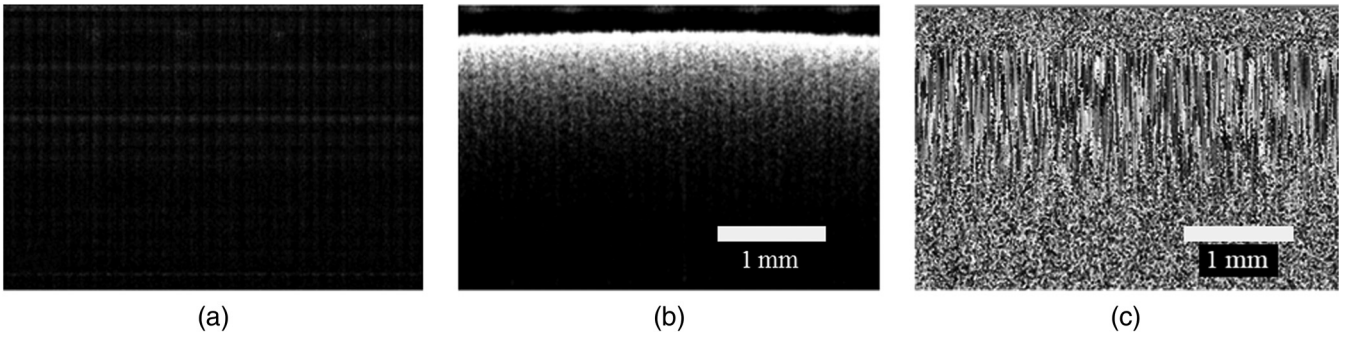

Fig. 4 (a) Fixed-pattern noise by blocking the sample arm. (b) Intensity image of a paperboard surface. Vertical artifacts are caused by periodic changes in output power. (c) Phase-resolved Doppler image of a finger. Scale bar is 1 mm.

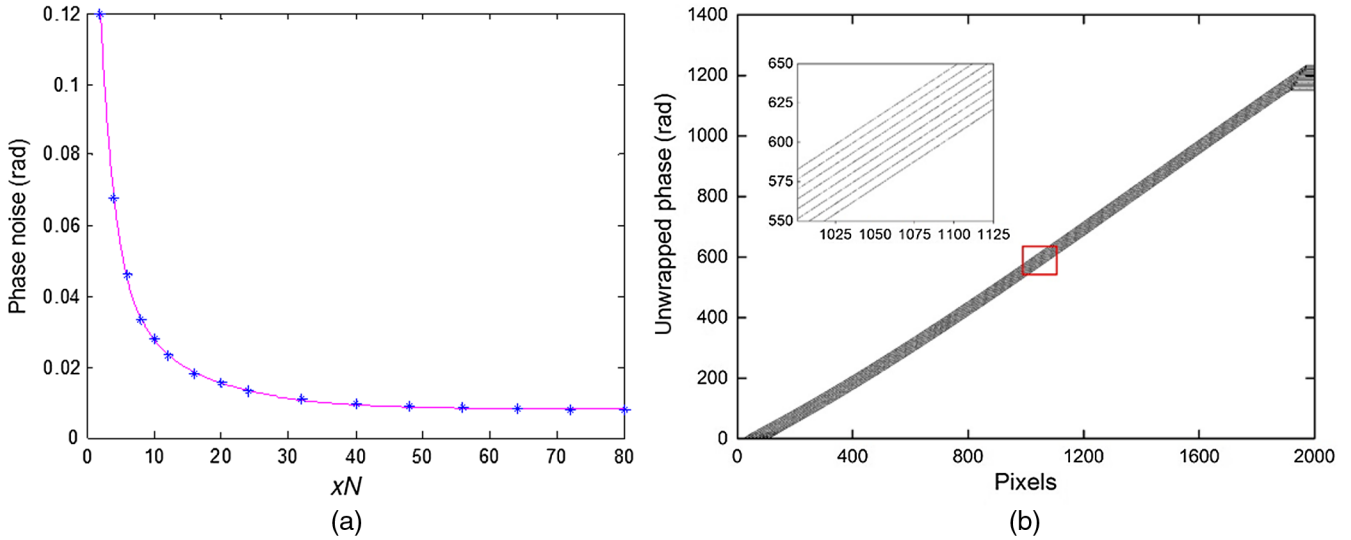

Fig. 5 (a) Relationship between signal extension multiple and phase noise of MZI signals; the magenta curve is the fitted curve. (b) Unwrapped phase curves for the 1000 MZI signals. The magnified section in the red box is plotted in the top-left corner.

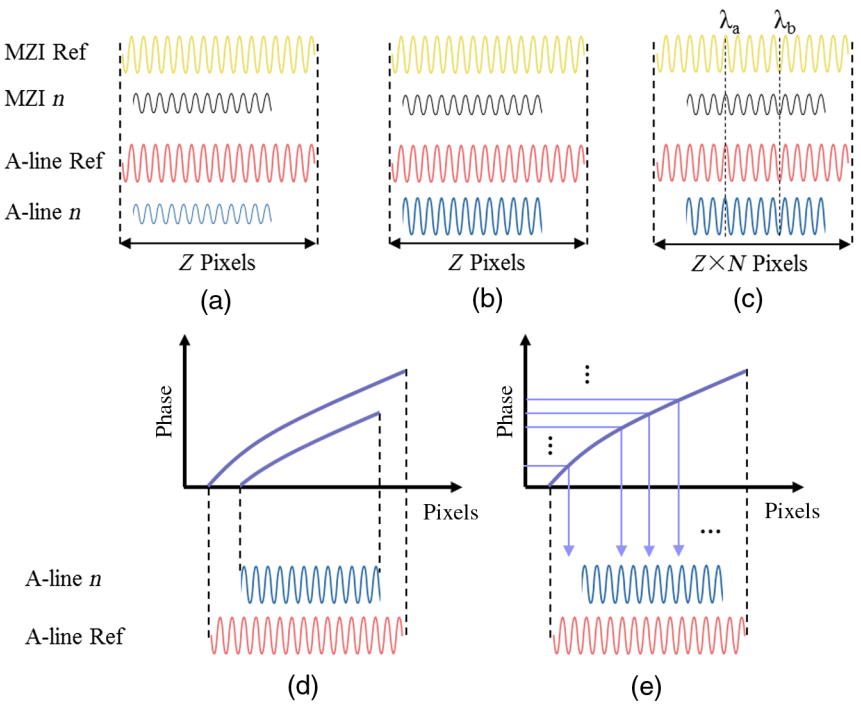

Fig. 6 (a) Reference MZI and other MZI signals, and the corresponding A-lines. (b) Normalization of all amplitudes of A-lines. (c) Extended signal that was already aligned. (d) Aligned A-line downsampled from (c) and corresponding to the unwrapped phase curve of the MZI signal. (e) Resampling and linearization of the A-lines using the unwrapped phase curve of the MZI signal with the maximum sweep range.

Phase correction is also needed to obtain flow information about the sample.

A human finger was also imaged to demonstrate the efficacy of our amplitude correction and phase correction method. The intensity image with the amplitude correction [Fig. 8(b), including 1280 A-lines] has a higher contrast compared to that without correction [Fig. 8(a)]. Figures 8(c) and 8(d) were obtained by subtracting (b) and (e) from (a) and (d), respectively, to visualize the vertical artifacts, which are marked by the green ordinate. There were ~42 fringes in 1280 A-lines, and fitting the results indicated that amplitude fluctuation frequency was ~660 Hz.

3.2 *Phase Stability Analysis*

Phase stability in an OCT system depends on the level of phase noise, which is described by the standard deviation of the phase

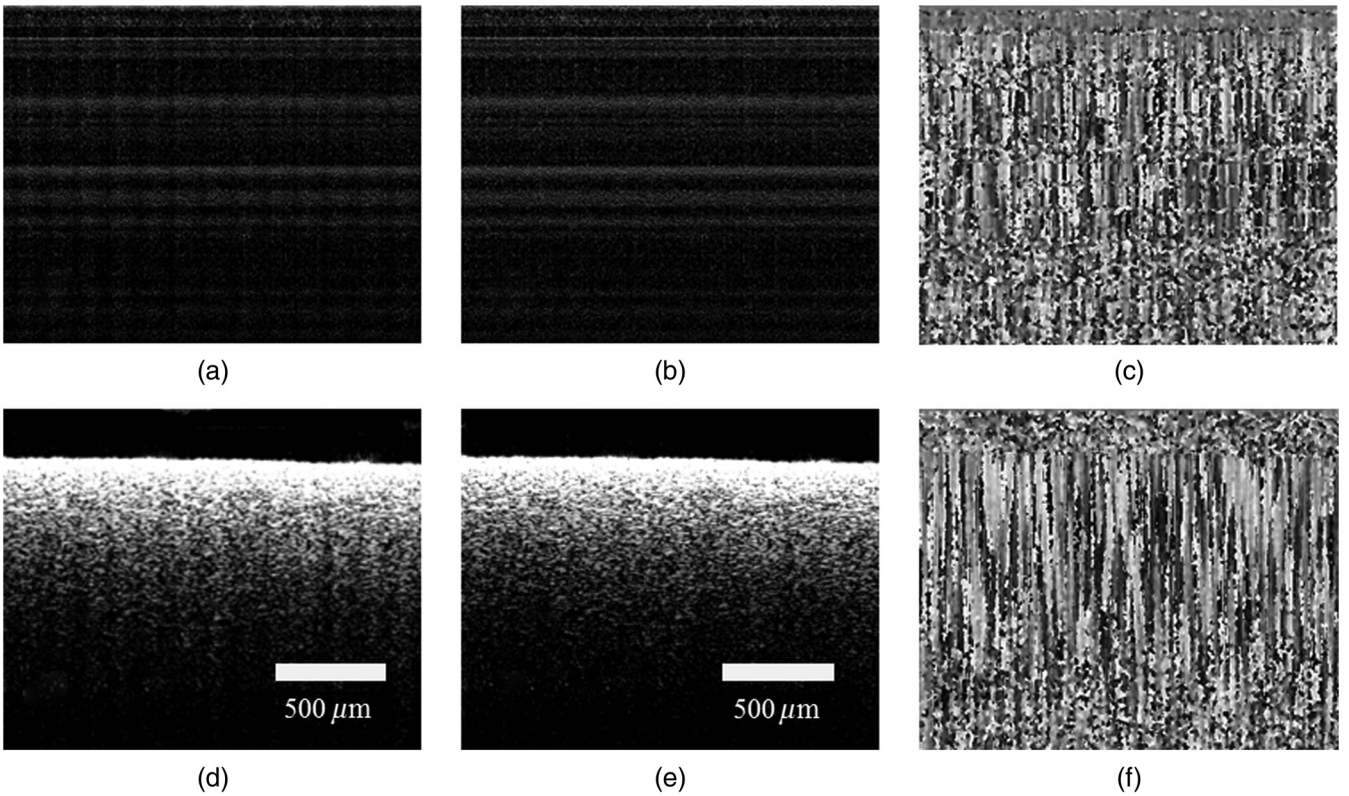

Fig. 7 Fixed-pattern noise (a) without amplitude correction and (b) with amplitude correction and (c) phase-resolved Doppler image. Paperboard image (d) without amplitude correction and (e) with amplitude correction and (f) phase-resolved Doppler image. Scale bar is 500 μm.

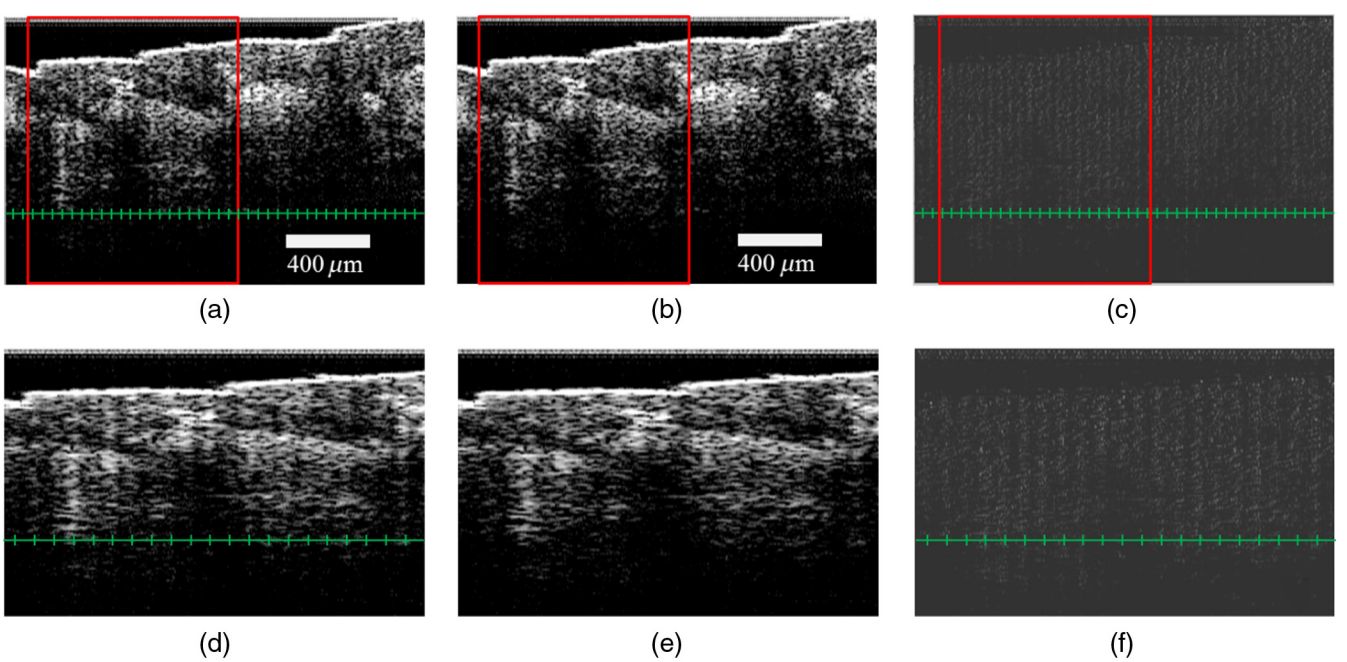

Fig. 8 Intensity image of a human finger (a) without amplitude correction and (b) with amplitude correction. Image (d) and (e) taken from the red box shown in (a) and (b), respectively. Image (c) shows differences between (a) and (b), while (f) shows differences between (d) and (e). The vertical fringes are indicated by green coordinate. Scale bar is 400 μm.

difference, $\Delta\varphi$, among adjacent A-lines, as measured on a stationary mirror.[16]

Without additional phase noise derivation, such as interference signal misplacement, the phase noise is determined by the signal-to-noise ratio (SNR), sample depth, and calibration signal[7]

$$\sigma^2_{\Delta\varphi} = \frac{1}{\mathrm{SNR}_s} + \left(\frac{Z_s}{Z_c}\right)^2 \frac{1}{\mathrm{SNR}_c}, \quad (1)$$

where SNR_s is the SNR of the sample at depth Z_s and SNR_c is the SNR of MZI at depth Z_c.

To characterize the limits of our phase correction method, 40 was chosen as the extension multiple.

20,000 successive A-lines on a stationary mirror were measured and acquired to count phase differences. Standard deviation of $\Delta\varphi$ was 3.9 mrad, which is close to the theoretical value of 3.6 mrad that was calculated using Eq. (2), when the mirror SNR was 49 dB at a depth of 1.01 mm (98 pixels) and SNR_c was 56 dB at a depth of 2 mm (194 pixels). The phase difference distribution with a standard deviation of 3.9 mrad is plotted in Fig. 9. This result also indicates that the polygon tunable laser had a consistent wavelength distribution over time, because wavelength distribution consistency determines the shape consistency of the MZI signal and, thus, the precision of the offset value obtained by cross correlation.

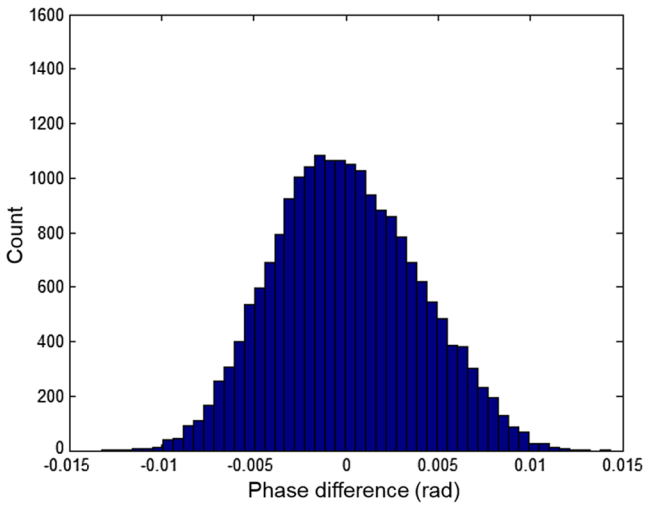

Fig. 9 Distribution of the phase difference measured from 20,000 A-lines at mirror depth.

3.3 *Flow Imaging In Vivo*

The phase-resolved Doppler flow imaging technology relies only on the phase information of the interference signal, and it assumes that successive A-lines have the same structure; a lateral scan will introduce extra phase noise, which is dominated by the lateral displacement among successive A-lines.[17] Therefore, images were acquired by dense lateral sampling, and 1280 A-lines were scanned with a 2-mm lateral displacement. The flow image without the phase correction was clearly incorrect [Fig. 10(e)] because our polygon tunable laser had a large phase error. After the phase correction, the image became smooth, and a blood vessel could be identified.

3.4 *Optical Microangiography for a Vascular Network Model*

The OMAG algorithm utilizes both the phase and intensity information of the OCT interference signal. Therefore, phase instability and output power fluctuations in a polygon tunable laser will prevent the resolution of static tissues and moving particles.

To verify our correction method, we pumped milk into a vascular network model with constant speed and then acquired a three-dimensional (3-D) data set ($3 \times 4 \times 1.3$-mm dense sampling was implemented in the B-scan direction). The vascular model and experimental device are showed in Fig. 11.

Then, a high-pass filter based on differential operation[18] was used to separate the static background and moving milk

$$I_{\mathrm{flow}}(t_i, k) = I(t_i, k) - I(t_{i-1}, k), \quad (2)$$

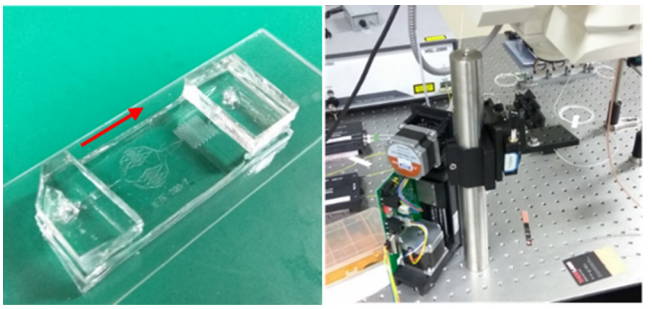

Fig. 11 (a) Photo of the vascular model. The widths of each branch are 500, 250, 100, 50, and 20 μm when height is 100 μm. The flow direction is indicated by red arrow. (b) Experimental platform.

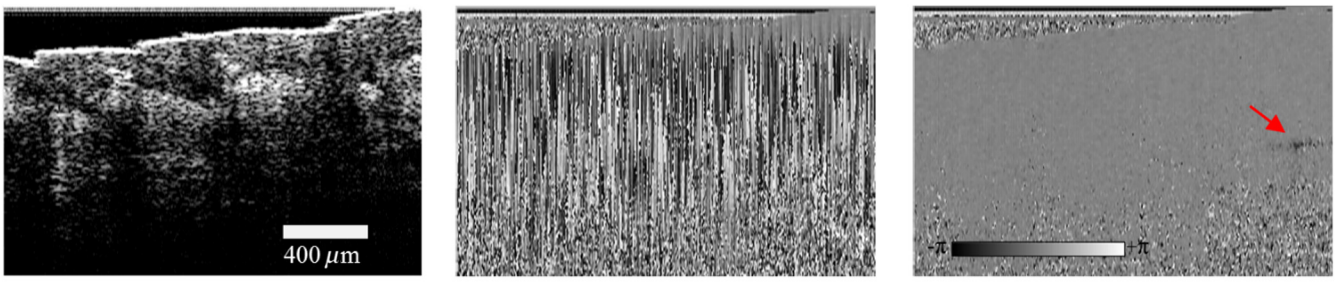

Fig. 10 (a) Intensity image of human finger. (b) Flow image without phase correction; the flow information is clearly incorrect. (c) Flow image with phase correction and an extension multiple of 16; a blood vessel is indicated by the red arrow. Scale bar is 400 μm.

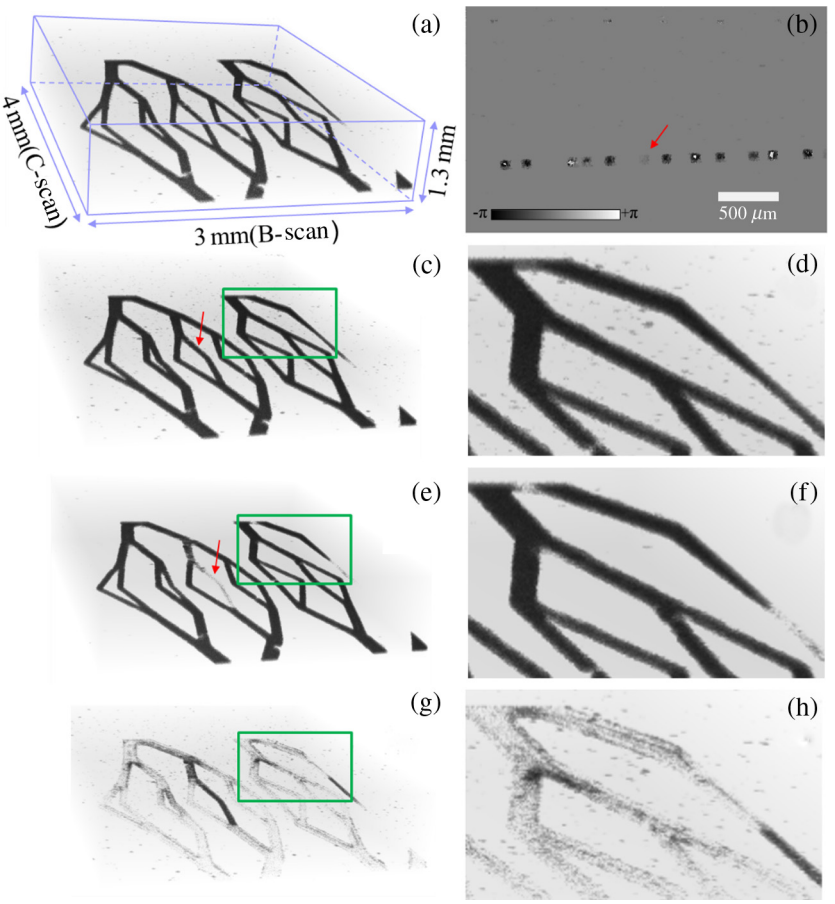

Fig. 12 (a) Three-dimensional intensity image of a vascular network model ($1280 \times 500 \times 335$ pixels, $3 \times 4 \times 1.3$ mm). (b) Flow image at frame index 261. Red arrow indicates that the speed of the milk at this position was very low. (c) OMAG image without amplitude and phase correction. (e) OMAG image with phase correction. Static impurities and milk (red arrow) were almost eliminated. (g) 3-D image of the static background obtained by subtracting (e) from (a). (d), (f), and (h) are magnified sections that appear in the green boxes in (c), (e), and (g), respectively.

where I_{flow} represents the optical intensity signal from the moving particles, i is the index of the A-lines, and k is the wavenumber.

Static impurities were present in the OMAG image without amplitude and phase correction [Figs. 12(c) and 12(d)]. After correction, static impurities were eliminated from the OMAG image [Figs. 12(e) and 12(f)]. In our data set, milk within a particular capillary had a very low speed, according to the flow image [red arrow in Fig. 12(b)], and we assumed that this milk was static. Correcting the OMAG image enabled easier elimination of this static milk [red arrow in Fig. 12(e)]. By subtracting the OMAG image from the 3-D intensity image, we obtained the static background [Figs. 12(g) and 12(h)], in which capillary walls, impurities, and static milk are clearly shown.

4 Discussion

Braaf et al.[11] also used MZI signals to phase stabilize an SS-OCT system; therefore, we compared their method and the proposed method using the polygon tunable laser-based OCT. First, their method determines the initial resample position by analyzing the MZI signal phase curve and resampling all the MZI signals to linear k-space; some phase information is truncated when there is a sweep range fluctuation [Fig. 13(a)]. 6.91% of the wavenumber of the unwrapped phase curve, which has the largest sweep range, would not be used in our system. Then, the cross correlation was used to correct multi-2π shifts in wavenumber, and the corrected MZI phase curve was used to resample and phase stabilize corresponding A-lines. However, the

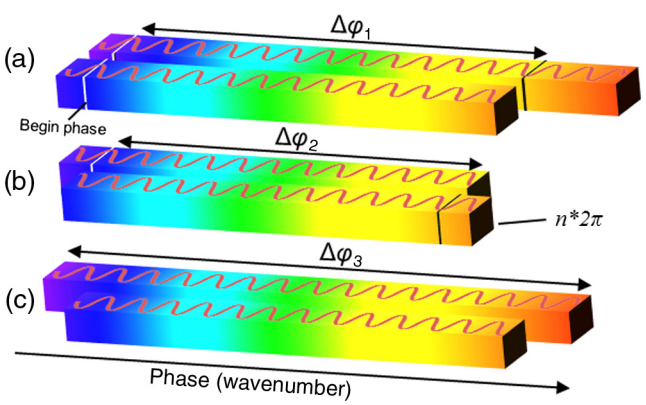

Fig. 13 MZI signals plotted with linear phase (wavenumber). (a) and (b) Phase stabilization by Braaf et al. method, only $\Delta\varphi_2$ wavenumber range phase information can be used, and (c) phase stabilization by proposed method, all phase information can be used.

multi-2π shift in k-space also leads to phase information loss during resampling [Fig. 13(b)], and the loss was related to the difference between the first points of the wavenumber of the two signals in our system: 3.66% of the wavenumber of the unwrapped phase curve, which has the largest sweep range. Hence, only 89.43% of the wavenumber of the phase curve was used after implementing their method. Based on the discrete Fourier transform, frequency resolution (computational axial resolution in OCT) is $\Delta f = fs/N$, where f_s is the sampling rate and N is the total number in the effective signal that is proportional to total phase increment $\Delta\varphi$. Hence, the proposed method can increase the resolution of the A-lines with a larger sweep range

$$\Delta z \propto \frac{1}{\Delta\varphi}, \tag{3}$$

where Δz is the image axial resolution. A static mirror of 30 mm away from zero frequency was acquired to obtain computational axial resolution, and the mirror peaks were at 378th pixels with the truncated signal and 403th pixels with fully used signal; thus, the computational axial resolutions were 7.937 and 7.444 μm, respectively. Hence, the axial resolution improvement limit was 0.493 μm. It should be noted that real axial resolution improvement does not usually reach this limit because the signal at the ends is not usually strong.

The method of Braaf et al. required resampling the MZI signal and then fit all the phase curves to the corresponding A-line; this may cost much computational time. The proposed method only requires fitting the phase curve of one MZI signal. We compared the multiplication number (real number) of their method and the proposed method with the same interpolate configuration and data (time domain interpolation,[19] cutoff width $L = 21$, resampling point number $N = 2048$, and A-line number $A = 1280$).

Table 1 indicated that the proposed method had fewer computational works, though it required more in FFT, because it only calculated the interpolation coefficient once, which reduced the needed computation.

Cross correlation and signal extension can both be implemented in the frequency domain. Therefore, the proposed method can be easily realized by graphics processing unit (GPU). It only took 56.1 s to phase stabilize and resample 500 B-scans with 1280 A-lines/B-scan when the extension multiple was 8 on a computer system equipped with a Tesla C2075 GPU.

The amplitude correction method could effectively smooth the intensity image that was influenced by output power fluctuation, but it should be noted that the SNR of each A-line was not changed, because the noise was also scaled. In addition to polygon tunable laser-based OCT, this method can theoretically be used for other OCT systems with problems that may lead to the interference amplitude being wholly changed in a swept cycle. However, this method may be unprecise if only a part of amplitude of the signal is changed, because the average envelope value of MZI signals can only represent the relative average amplitude of an A-line.

5 Conclusion

We found and demonstrated the instability problems in a polygon tunable laser, including fluctuations of the sweep range and output power, using the amplitude envelope and phase information of the Hilbert transform of MZI signals. This problem causes difficulty in intensity imaging and phase stabilization. The proposed amplitude method effectively eliminated the vertical artifacts, which is important for distinguishing between biological tissues during biomedical imaging. We also proposed a phase correction method based on zero-padding in the frequency domain and cross correlation. Theoretic analysis indicated that it could fully utilize the phase information of the MZI signal to improve the resolution of the flow and intensity images; the phase noise was close to the theoretical value and the flow information could be identified. The correction method is used for polygon tunable laser-based OCT system, and it may also be applied to other kinds of laser-based OCT and help improving the image quality with the development of tunable laser technology and improvements in the consistency of wavelength distribution.

Disclosures

No conflicts of interest, financial or otherwise, are declared by the authors.

Acknowledgments

The work was supported by the National Scientific Instrument and Equipment Development Project (No. 2016YFF0102000), the Strategic Priority Research Program of the Chinese Academy of Sciences (No. XDB02060000), the Frontier Science Research Project of the Chinese Academy of Sciences (No. QYZDB-SSW-JSC03), the Jiangsu Province Science Fund for Distinguished Young Scholars (No. BK20060010), and the National Natural Science Foundation of China (Nos. 61675226 and 61378090).

Table 1 Multiplication number of main processing steps in Braaf et al. method and proposed method when extension multiple is 64.

Processing step	Braaf et al. method	Proposed method
FFT in cross correlation and extension	$(\log_2 N \times N/2 + \log_2 N \times N/2) \times A \times 4$	$[\log_2 N \times N/2 + \log_2(N \times M) \times N \times M/2] \times A \times 2 \times 4$
Coefficient calculation	$3 \times N/2 \times N \times L \times A$	$3 \times N/2 \times N \times L$
Multiplication in cross correlation	$N \times A$	$N \times A$
Interpolation	$2 \times N \times L \times A$	$N \times L \times A$
Total	169, 342, 402, 560	11, 713, 642, 496

References

1. S. H. Yun et al., "Motion artifacts in optical coherence tomography with frequency-domain ranging," *Opt. Express* **12**(13), 2977–2998 (2004).
2. J. W. You et al., "Pulsed illumination spectral-domain optical coherence tomography for human retinal imaging," *Opt. Express* **14**(15), 6739–6748 (2006).
3. S. H. Yun et al., "High-speed wavelength-swept semiconductor laser with a polygon-scanner-based wavelength filter," *Opt. Lett.* **28**, 1981–1983 (2003).
4. T. Huo et al., "Linear-in-wavenumber swept laser with an acousto-optic deflector for optical coherence tomography," *Opt. Lett.* **39**(2), 247–250 (2014).
5. Y. H. Zhao et al., "Phase-resolved optical coherence tomography and optical Doppler tomography for imaging blood flow in human skin with fast scanning speed and high velocity sensitivity," *Opt. Lett.* **25**, 114–116 (2000).
6. R. K. Wang et al., "Three dimensional optical angiography," *Opt. Express* **15**(7), 4083–4097 (2007).
7. B. J. Vakoc et al., "Phase-resolved optical frequency domain imaging," *Opt. Express* **13**(14), 5483–5493 (2005).
8. B. Baumann et al., "Total retinal blood flow measurement with ultrahigh speed swept source/Fourier domain OCT," *Biomed. Opt. Express* **2**(6), 1539–1552 (2011).
9. J. Zhang and Z. Chen, "In vivo blood flow imaging by a swept laser source based Fourier domain optical Doppler tomography," *Opt. Express* **13**, 7449–7457 (2005).
10. Y.-J. Hong et al., "High penetration swept source Doppler optical coherence angiography by fully numerical phase stabilization," *Opt. Express* **20**(3), 2740–2760 (2012).
11. B. Braaf et al., "Phase- stabilized optical frequency domain imaging at 1-μm for the measurement of blood flow in the human choroid," *Opt. Express* **19**(21), 20886–20903 (2011).
12. G. Liu et al., "Postprocessing algorithms to minimize fixed-pattern artifact and reduce trigger jitter in swept source optical coherence tomography," *Opt. Express* **23**(8), 9824–9834 (2015).
13. Y. Yasuno et al., "Three-dimensional and high-speed swept-source optical coherence tomography for in vivo investigation of human anterior eye segments," *Opt. Express* **13**(26), 10652–10664 (2005).
14. M. Gora et al., "Ultrahigh-speed swept source OCT imaging of the anterior segment of human eye at 200 kHz with adjustable imaging range," *Opt. Express* **17**(17), 14880–14894 (2009).
15. W. Drexler and J.G. Fujimoto, *Optical Coherence Tomography: Technology and Applications*, pp. 190–197, Springer, Berlin (2008).
16. B. White et al., "In vivo dynamic human retinal blood flow imaging using ultra-high-speed spectral domain optical coherence tomography," *Opt. Express* **11**(25), 3490–3497 (2003).
17. B. Park et al., "Real-time fiber-based multi-functional spectral-domain optical coherence tomography at 1.3 μm," *Opt. Express* **13**(11), 3931–3944 (2005).
18. Z. Zhi et al., "Volumetric and quantitative imaging of retinal blood flow in rats with optical microangiography," *Biomed. Opt. Express* **2**(3), 579–591 (2011).
19. Y. Zhang et al., "Time-domain interpolation for Fourier-domain optical coherence tomography," *Opt. Lett.* **34**(12), 1849–1851 (2009).

Biographies for the authors are not available.